Ionothermal Carbonization of Sugarcane Bagasse in 1-Alkyl-3-methylimidazolium Ionic Liquids: Insights into the Role of the Chloroferrate Anion

Soha Aldroubi, Pascale Guiffrey, Mohamed El-Sakhawy, Samir Kamel, Ibrahim Bou Malham, Peter Hesemann, Ahmad Mehdi, Nicolas Brun, Amine Geneste

Ionothermal carbonization of sugarcane bagasse in 1-alkyl-3-methylimidazolium ionic liquids: insights into the role of the chloroferrate anion

Soha Aldroubi,[a] Amine Geneste,[a] Pascale Guiffrey,[a] Mohamed El-Sakhawy,[b] Samir Kamel,[b] Ibrahim Bou Malham,[c] Peter Hesemann,[a] Ahmad Mehdi[a] and Nicolas Brun[a]*

[a]ICGM, Univ. Montpellier, CNRS, ENSCM, Montpellier, France.

[b]Cellulose and Paper Department, National Research Centre, Giza, Egypt.

[c]EREN, Faculté des Sciences IV, Université Libanaise, Zahlé, Liban.

KEYWORDS. Ionic liquid, halometallate, biomass, lignocellulose, carbonization, ionochar.

ABSTRACT. We report the ionothermal carbonization (ITC) of lignocellulosic biomass in imidazolium tetrachloroferrate ionic liquids (ILs) as an advantageous approach for the preparation of nanostructured carbonaceous materials, namely ionochars. In a previous study, we investigated the role of imidazolium cation and demonstrated the possibility of controlling both the textural and morphological properties of ionochars by cation engineering. Although essential for providing intermediate Lewis acidity and relatively high thermal stability, the role of the chloroferrate anion is still open to debate. Herein, we investigated the ITC of sugarcane bagasse and its main component, cellulose, in 1-alkyl-3-methylimidazolium ILs with different

chloroferrate anions. We identified anionic speciation and its impact on the properties of the IL by Raman spectroscopy, thermogravimetric analysis and differential scanning calorimetry. The obtained ionochars were characterized by gas physisorption, electron microscopy, Raman, FTIR and solid-state ^{13}C CP-MAS NMR spectroscopy. We show that the anionic species have a predominant impact on the textural and morphological properties of the ionochars.

INTRODUCTION. The conversion of abundant agrowastes into fuels, platform chemicals and materials is in line with the need to move away from unsustainable fossil resources and to expand the "renewable chemical space"[1]. In particular, nanostructured carbonaceous materials derived from agrowastes have been of great interest as they find potential applications in various fields such as energy storage[2-6], catalysis[7-9] and gas adsorption.[10-12] The morphology, the nanostructure and the porosity of the carbonaceous materials have a strong impact on their physico-chemical properties, which intimately determine their potential applications.[13] In this context, many synthetic approaches have been explored to design and engineer nanostructured carbonaceous materials from bio-derived precursors and raw agrowastes.[14] Conventional thermochemical processes, including pyrolysis and activation, have been widely reported to produce pyrogenic carbons including biochars for soil amendment[15] or activated carbons for wastewater treatment[16] and energy storage[17]. These processes have, however, major drawbacks among which a moderate to extremely poor carbonization yield (especially with cellulose-rich agrowastes), a limited coverage of surface functional groups and a weak control of textural and morphological properties.[18] To overcome these drawbacks, unconventional thermochemical processes have been proposed as sustainable alternatives, including hydro-[19], solvo-[20] and ionothermal carbonization[21].

Ionothermal carbonization (ITC) [21-24], which consists in the carbonization of organic matter in ionic liquids (ILs) media, is a parent process of hydrothermal carbonization (HTC)[25]. ITC has been proposed as a profitable and atom efficient alternative to convert agrowastes into nanostructured carbonaceous materials, namely ionochars[25]. In the same way as HTC, ITC of (ligno)cellulose runs at mild temperature (< 250 °C) and under autogenous pressure (< 20 bars) and involves very complex cascade reactions of hydrolysis, dehydration, decarboxylation, polymerization, and aromatization[19]. While HTC suffers from the weak dissolution of lignocellulose in water and often yields non-porous hydrochars with poor textural and morphological control, the use of wisely selected ILs offers broad control and versatility to the ITC process[22, 24, 26].

ILs are defined as salts that are liquid at a temperature below 100 °C and are known as task-specific solvents[27]. They usually consist of an organic cation in interaction with an inorganic anion, both governing their physico-chemical properties which can be easily modulated through molecular engineering[28]. ILs display singular properties such as almost zero vapor pressure, non-flammability and relatively high thermal stability. For these reasons, they have been considered as alternatives to volatile organic solvents[29]. In particular, some ILs display a good ability to dissolve and depolymerize cellulose[30-32], lignin[33-34] and even lignocellulose[35], especially those bearing a cation with short alkyl chains, such as 1-butyl-3-methylimidazolium $[C_4mim]^+$, and an anion with strong hydrogen-bond acceptance (HBA)[36], such as chloride and acetate[30]. Recently, imidazolium halometallate ILs, such as $[C_4mim]FeCl_4$, that were initially studied for their paramagnetic properties[37-38], demonstrated the ability to catalyze the selective depolymerization of lignin through the cleavage of γ-O ester[33] and β-O-4 ether bonds[39]. Taking advantage of its intermediate Lewis acidity and its relatively high thermal stability, $[C_4mim]FeCl_4$ was also used

for the ITC of polysaccharides[40] and lignocellulosic agrowastes[23-24, 26], yielding highly porous ionochars with high mass and carbon yields. Xie et al. demonstrated the benefits of ITC in $[C_4mim]FeCl_4$ at 180 °C as a pre-treatment of Jujun grass before chemical activation with KOH[23]. The as-obtained ionochar-derived activated carbons displayed superior performance as electrode materials for supercapacitors. In a recent study, our group applied the ITC process to a wet agrowaste, i.e., cocoa bean shells. We demonstrated the high stability of $[C_4mim]FeCl_4$ during ITC at 240 °C and its recyclability was clearly evidenced. The subsequent physical activation of the as-obtained ionochars allowed producing activated carbons with remarkable carbon dioxide (CO_2) uptake of 4.4 mmol g^{-1} at 25 °C and 1 bar.

More recently, we demonstrated the role of the cationic structure of imidazolium tetrachloroferrate ILs in the ITC of (ligno)cellulose[26]. Depending on the side groups on imidazolium, e.g., alkyl chains with different lengths and/or benzyl groups, we demonstrated the possibility to control both textural and morphological properties of the ionochars[26]. Ionochars with high specific surface areas (up to 800 m^2 g^{-1}) and pore volumes (up to 0.8 cm^3 g^{-1}) were obtained without subsequent pyrolysis or activation. The way in which the anion (i.e., Cl^-, $FeCl_4^-$, BF_4^- and Tf_2N^-) associated with $[C_4mim]^+$ impacts on the ITC of lignocellulose was also evidenced in the literature[22, 24]. P. Zhang et al. suggested that ILs with large anions favour the formation of porosity in ionochars.[22] Although of great fundamental interest, this study reported an ionochar starting from sugarcane bagasse with poor specific surface area and low pore volume of ca. 35 m^2 g^{-1} and 0.15 cm^3 g^{-1}, respectively. Besides, the ILs reported were relatively unstable at 200 °C, yielding heteroatom-doped ionochars. Finally yet importantly, this last study was limited to simple, metal-free anions. The case of halometallate anions, and more specifically chloroferrate anions[41-42], is more complex as it involves anion speciation and dynamic equilibria

with monomeric and/or oligomeric anionic species of varying nuclearity and coordination number[43-44]. Although essential for providing intermediate Lewis acidity and relatively high thermal stability, the role of the chloroferrate anion is still open to debate. A systematic investigation of the composition and physico-chemical properties of 1-alkyl-3-methylimidazolium chloroferrate ILs has never been proposed in the literature. This is all the more true when it comes to the use of these ILs in ITC. The simultaneous influence of the 1-alkyl-3-methylimidazolium cation and the chloroferrate anion on the carbonization of biomass has never been investigated.

Herein, we propose an original and systematic study to fill this knowledge gap and to reach a better understanding. We investigated the role of the chloroferrate anion in the ITC of lignocellulose in imidazolium-based ILs. We prepared a series of 1-alkyl-3-methylimidazolium ILs with different $[C_nmim]^+$ cations (with $2 < n < 8$; Scheme 1) and different chloroferrate anions by modifying the $FeCl_3/[C_nmim]Cl$ molar ratio from 0.5 to 2. We proposed a systematic evaluation of the nature of the chloroferrate anion to assess its effect on the ITC of (ligno)cellulose. The 1-alkyl-3-methylimidazolium chloroferrate ILs were characterized by Raman spectroscopy and differential scanning calorimetry (DSC) to identify the nature of the chloroferrate anions and its impact on the properties of the IL. We selected sugarcane bagasse from Egypt as a raw lignocellulosic agrowaste model, as sugarcane represents a global annual production of ca. 1.9 billion tons[45]. Sugarcane bagasse (or cellulose) was treated at 240 °C for 20 h in ca. 10 mL of IL (Scheme 1). After washing and oven drying, ionochars were collected and thoroughly characterized by gas sorption (N_2 at 77 K and CO_2 at 273-323 K), electron microscopy (SEM and TEM), energy-dispersive X-ray spectroscopy (EDX), elemental analysis,

Raman, FTIR and ^{13}C solid-state CP-MAS NMR spectroscopy. We showed that the anionic species have a predominant impact on the textural and morphological properties of the ionochars.

EXPERIMENTAL SECTION

Materials

1-ethyl-3-methylimidazolium chloride ([C_2mim]Cl, 99%), 1-butyl-3-methylimidazolium chloride ([C_4mim]Cl, 99%), 1-hexyl-3-methylimidazolium chloride ([C_6mim]Cl), and 1-octyl-3-methylimidazolium chloride ([C_8mim]Cl) were purchased from Iolitec (Germany). Sigmacell cellulose (type 50, 50 μm) and iron (III) chloride hexahydrate ($FeCl_3.6H_2O$, 97%) were purchased from Sigma-Aldrich. Sugarcane bagasse was donated by Quena Company for Paper Industry (Egypt), dried, ground and sifted (> 100 μm). All reagents were used without further purification.

Preparation of 1-alkyl-3-methylimidazolium chloroferrate ILs

ILs were prepared by heating at 80 °C under agitation for 6 hours a mixture of [$C_n$mim]Cl and $FeCl_3.6H_2O$ at different molar ratios, x (from 0.5 to 2.0). At the end of the reaction, two phases were obtained: a lower phase comprising the expected 1-alkyl-3-methylimidazolium chloroferrate IL and an upper phase containing water. Water was removed *via* rotary evaporation at 60 °C and 10 mbar for 4 hours and subsequent lyophilization for 12 hours. The 1-alkyl-3-methylimidazolium chloroferrate ILs were named **[$C_n$mim]Fe-x**, with n, the alkyl chain length in [$C_n$mim]$^+$ from 2 to 8, and x, the $FeCl_3$/[$C_n$mim]Cl molar ratio from 0.5 to 2.

ITC of sugarcane bagasse and cellulose

In a standard procedure, 1 g of ground and sifted bagasse (> 100 μm) was mixed with 40.2 mmol of IL, sealed in a Teflon lined autoclave (23 mL) and heated at 240 ^{0} C for 20 h under

autogenous pressure. After quenching in cold water and cooling down to room temperature, samples were washed once with ultrapure water (150 mL, 18.2 MΩ.cm), once with water/ethanol mixture (50:50, v/v) (150 mL) and once with pure ethanol (150 mL), filtered, and dried at 80 ^{0} C overnight in a vacuum drying oven (Scheme 1).

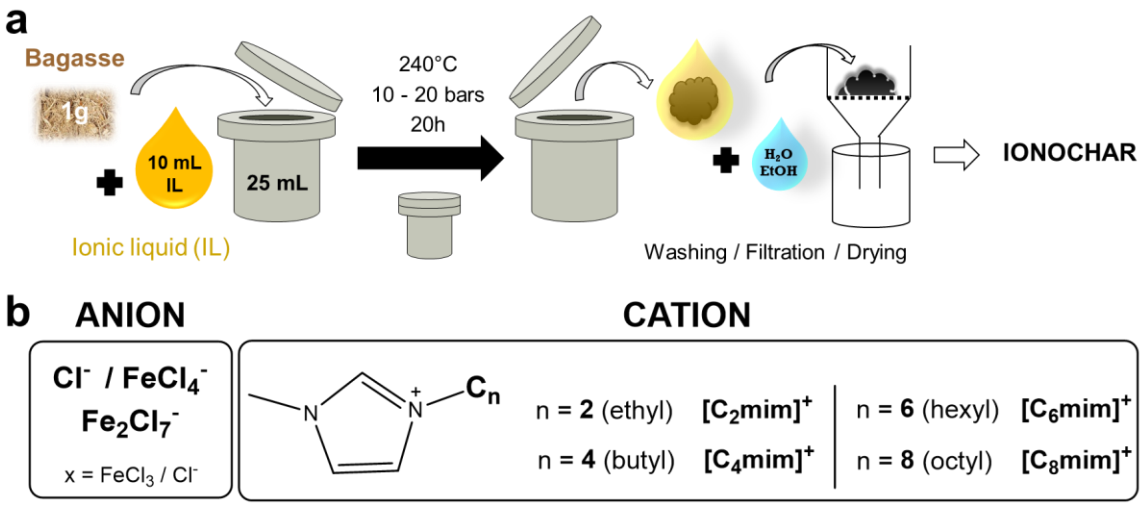

Scheme 1. (a) Schematic representation of the ionothermal carbonization process (ITC) with (b) the chemical structure of the different ILs studied herein.

The ionochars prepared from sugarcane bagasse were named **C_nm-Bg-x**, with n, the alkyl chain length in $[C_nmim]^+$ from 2 to 8, and x, the $FeCl_3$/$[C_nmim]Cl$ molar ratio from 0.5 to 2. Similar ITC experiments were carried out with commercial cellulose; the ionochars were named **C_nm-C-x**. HTC in 10 mL of ultrapure water was also carried out on bagasse (1 g) and on cellulose (1 g) in similar conditions, yielding the hydrochars named **HTC-Bg** and **HTC-C**.

Mass and carbon yields

The mass yield (y_m) and the corrected mass yield (y_{mc}) were calculated as follows:

$$\boldsymbol{Y_m}\ (\%) = \frac{\boldsymbol{Mass\ of\ dried\ char\ (g)}}{\boldsymbol{Mass\ of\ dried\ biomass\ (g)}} \times \mathbf{100}$$

$$\boldsymbol{Y_{mc}}\ (\%) = \frac{\boldsymbol{Mass\ of\ dried\ char - Mass\ of\ residual\ IL\ (g)}}{\boldsymbol{Mass\ of\ dried\ biomass\ (g)}} \times \mathbf{100}$$

The residual IL corresponds to any compound present in the dried char and coming from the salt ($FeCl_3$) or the IL ($[C_n mim]Cl$), *i.e.*, iron, chloride and nitrogen excess. Iron and chloride contents were determined by SEM-EDX. Nitrogen content was determined by elemental analysis. The nitrogen excess coming from the IL was determined by subtracting the nitrogen coming from the initial biomass. **HTC-Bg** and **HTC-C** were used as references.

The carbon yield (Y_c) was calculated as follows:

$$\boldsymbol{Y_c}\ (\%) = \boldsymbol{Y_m}\ (\%) \times \frac{\boldsymbol{C\ content\ in\ dried\ char\ (wt.\%)}}{\boldsymbol{C\ content\ in\ dried\ biomass\ (wt.\%)}} \times \mathbf{100}$$

Characterization

Differential scanning calorimetry (DSC) experiments were performed on a STARe® DSC1 instrument (METTLER TOLEDO). The sample (ca. 10–20 mg) was weighed on a high-precision balance (0.00001 mg) into a 40 µL aluminium crucible. The crucible was then sealed using a press with a pre-drilled aluminium lid of the same diameter as the crucible. The crucible containing the sample was then positioned in the measurement cell, on the sensor (at room temperature) next to an empty crucible acting as a reference. The lid of the furnace containing the measuring cell was then closed. DSC experiments were performed under nitrogen flow atmosphere (200 mL min^{-1}). The temperature program was as follows: first heating from 25 to 150 °C (at a rate of 5 °C min^{-1}), first cooling from 150 to -150 °C (5 °C min^{-1}), isothermal stage at -150 °C for 10 min, and second heating from -150 to 150 °C (5 °C min^{-1}). Thermogravimetric

analyses (TGA) were performed on a STA 449 F1 instrument (Netzsch) from 25 to 700 °C at a rate of 10 °C min^{-1} under argon flow atmosphere (60 mL min^{-1}).

Raman spectroscopy was carried out on a Renishaw inVia Raman microscope with a 532 nm laser excitation. A laser power of 3 mW (10%) and an acquisition time of 2 s were used for the ionic liquids. A laser power of 0.3 mW (1%) and an acquisition time of 40 s were used for the ionochars. FTIR spectroscopy was performed in attenuated total reflectance (ATR) mode on a PerkinElmer Spectrum Two spectrometer.

GC-MS was performed on a Shimadzu QP2010SE gas chromatograph-mass spectrometer with a Phenomenex Zebron ZB-5ms column (30m x 0.18mm x 0.18µm). Injection: Split 1:30 at 250 °C. Oven program: 50 °C (Hold 2 min), 50-280 °C at 22 °C min^{-1} (Hold 2 min).

Immersion calorimetry was performed on a C80 calorimeter from Setaram Instrumentation. For each experiment, 300 mg of sugarcane bagasse was weighed and transferred in the lower part (a small 1-mL cylinder) of an empty fragile-tip glass ampoule via a custom-made glass funnel in its upper part (a 10-cm cylindrical tube). The ampoule filled with sugarcane bagasse was then degassed at 80 °C for 2 h (with a vacuum of ca. 10^{-2} mbar. Once degassing was completed, the ampoule was vacuum-sealed using a dual-flame (butane-oxygen) welding unit. The vacuum was maintained during the sealing process to facilitate the retraction of the liquefied glass onto itself, allowing the ampoule to close naturally thanks to the internal vacuum. Once the ampoule was closed, the lower part was separated from the upper part. The sealed ampoule was then gently positioned (with the fragile tip downwards and the weld upwards) in a 12.5 mL stainless steel cylindrical cell previously filled with 3 mL of ionic liquid. The cell was then clipped to a rod fitted with a sliding hammer and placed in the calorimeter, which was kept at 80 °C. The

reference cell contains only the ionic liquid. Once the temperature and heat flow stabilized (2 h), the fragile tip of the ampoule was broken with the hammer, allowing the sugarcane bagasse and the ionic liquid to mix. The vacuum sucks the liquid into the ampoule, which encourages contact and therefore dissolution. The heat flow was recorded for 3 h.

Scanning electron microscopy (SEM) analyses were performed on a Hitachi S-4800 electron microscope. SEM-EDX (Energy Dispersive X-ray spectroscopy) analyses were performed on a Zeiss EVO HD15 electron microscope. Transmission electron microscopy (TEM) analyses were performed on a JEOL 1200 microscope from MEA (Univ. Montpellier). N_2 (at 77 K) and CO_2 (at 273, 298 and 323 K) physisorption experiments were carried out on a Micromeritics 3Flex apparatus. Ionochars were degassed at 150 °C for 6 h under high vacuum (*ca.* 0.1 Pa) before physisorption measurements. BET equivalent specific surface area (SSA_{BET}) was determined applying the BET equation in the relative pressure range from 10^{-2} to 10^{-1}, determined with the superior limit given by the maximum of the Rouquerol curve. Micropore specific surface area (SSA_{micro}), micropore volume (V_{micro}) and external volume (V_{ext}) were determined from the t-plot method (Thickness equation: Harkins and Jura). To determine the isosteric heats of adsorption, we applied the Clausius-Clapeyron equation (see equation 1 below) to CO_2 adsorption isotherms obtained at the three different temperatures:

$$\Delta \mathbf{H_{ads}} = \mathbf{R} \left(\frac{\partial \ln p}{\partial \frac{1}{T}} \right)_{\theta} \qquad \text{(equation 1)}$$

with R, the molar gas constant (R = 8.314 J mol^{-1} K^{-1}); Θ, the recovery rate, *i.e.*, the fraction of active sites occupied by the CO_2 molecules or mmol of CO_2 adsorbed per gram of ionochar; T, the temperature, K; and p, the absolute pressure, kPa.

RESULTS AND DISCUSSION

As mentioned above, 1-alkyl-3-methylimidazolium chloroferrate ILs display advantageous properties that have encouraged their use for ITC such as intermediate Lewis acidity and relatively high thermal stability[21, 23-24]. However, a systematic study of their physical properties depending on both the cationic structure and the anionic species has not been proposed yet. Herein, we prepared a series of 1-alkyl-3-methylimidazolium ILs from four different $[C_nmim]^+$ cations (with $2 \leq n \leq 8$; Scheme 1) and from various $FeCl_3/[C_nmim]Cl$ molar ratios, x, ranging from 0.5 to 2. The as-obtained ILs were named **$[C_n$mim]Fe-x**. For n = 2 and 4, we could prepare homogeneous, stable chloroferrate ILs for $x \leq 1.5$ (Figure 1a). For n = 2, homogeneous ILs were also obtained at higher ratios, *i.e.*, with x = 1.8 and 2, but phase separation and subsequent precipitation were observed after a few hours at room temperature, without impeding their use. When increasing the alkyl chain length from ethyl to octyl, the phase separation phenomenon occurred at lower $FeCl_3/[C_nmim]Cl$ molar ratios. Then, for n = 6 and 8, homogeneous liquids were obtained for $x \leq 1$, while highly heterogeneous mixtures were obtained for $x > 1$. Based on these observations, we limited our study to the most homogeneous ILs that showed limited phase separation and/or precipitation over time.

The ILs of the **$[C_2$mim]Fe-x** series were characterized by Raman spectroscopy and DSC. At first glance, it is clear that the $FeCl_3/[C_nmim]Cl$ molar ratio has an effect on the anionic speciation and on the physico-chemical properties of the IL; its colour changes from rusty orange to yellow by increasing the ratio from 0.5 to 1, then from yellow to black by increasing the ratio from 1 to 1.5 (Figure 1a). In the literature, it has been shown that tetrachloroferrate anions $[FeCl_4]^-$ predominates for $x \leq 1$, while heptachlorodiferrate anions $[Fe_2Cl_7]^-$ coexist with $[FeCl_4]^-$ for $x > 1$. This property was observed experimentally by Raman spectroscopy for **$[C_4$mim]Fe-x** ILs and

confirmed by *ab initio* calculations[41-42]. Herein, Raman spectroscopy conducted on the **[C$_2$mim]Fe-x** series showed similar features (Figure 1b).

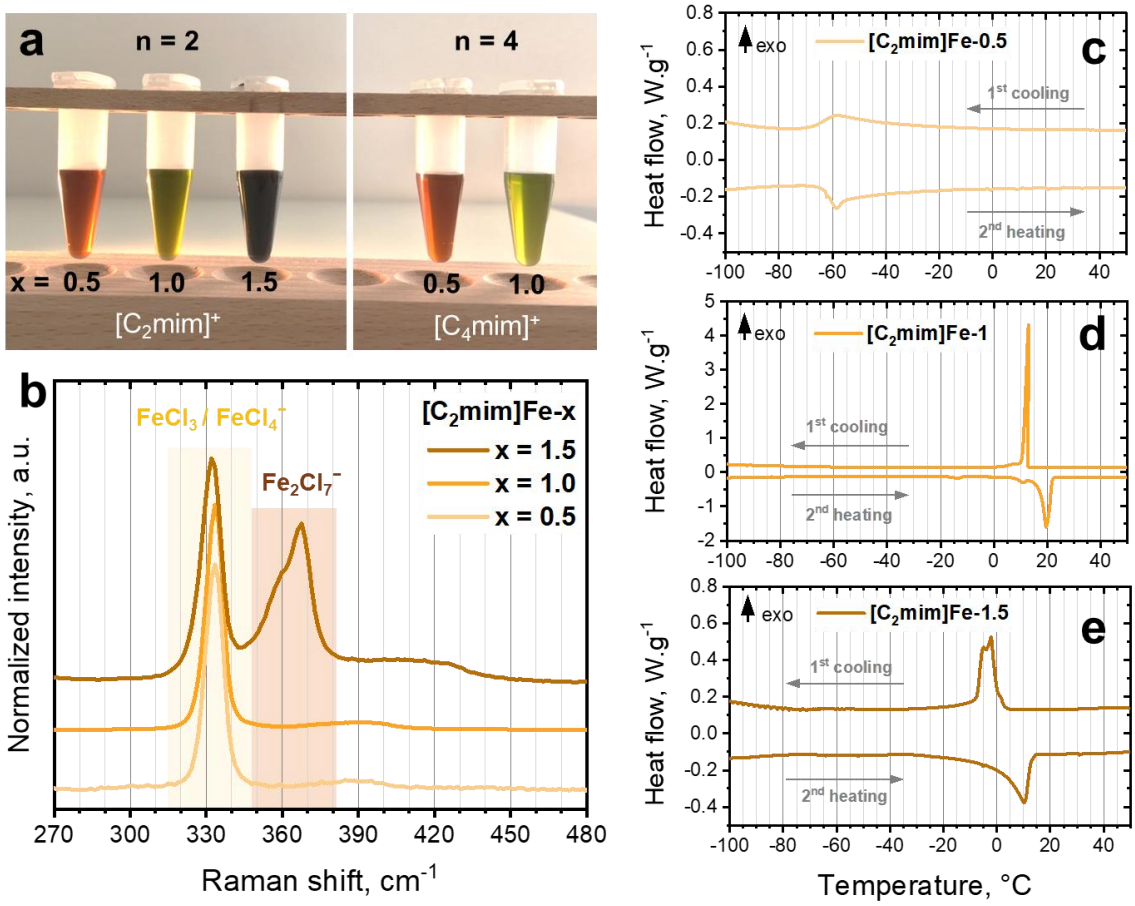

Figure 1. (a) Picture of **[C$_n$mim]Fe-x** ILs. (b) Raman spectra and (c, d, e) DSC thermograms of three ILs of the **[C$_2$mim]Fe-x** series.

The spectra of **[C$_2$mim]Fe-0.5** and **[C$_2$mim]Fe-1** displayed an intense peak centred at 333 cm^{-1} together with a weaker contribution at *ca.* 390 cm^{-1} related to the T_2 and A_1 symmetry vibrations of the T_d structure of $[FeCl_4]^-$.[41] As expected, identical spectra were obtained for **[C$_n$mim]Fe-x** ILs with x ≤ 1 (Figure S1). It should be noted that the peak centred at 333 cm^{-1} might be also related to anhydrous iron(III) chloride, $FeCl_3$ (Figure S2). However, anhydrous $FeCl_3$ quickly hydrates to aquo-chloro complexes when exposed to air, as shown by Raman spectroscopy

(Figure S2). This behaviour was not observed with **[$C_n$mim]Fe-x ILs**, that are known to be relatively moisture-stable by their hydrophobic character[43]. As for **[C_2mim]Fe-1.5**, we observed three new contributions in addition to the two peaks described above with $x \leq 1$. The intense peak centred at 368 cm^{-1}, the shoulder centred at 360 cm^{-1} and the weaker, broader contribution centred at *ca.* 420 cm^{-1} were all assigned to symmetry vibrations of the C_2 structure of $[Fe_2Cl_7]^-$ [41]. As mentioned above, **[C_2mim]Fe-x** with $x > 1.5$ gave unstable ILs with phase separation and subsequent precipitation after a few hours. This feature was confirmed by Raman spectroscopy as we observed a fast decrease in the intensity of the two peaks centred at 360 and 368 cm^{-1} with time, especially for **[C_2mim]Fe-2** (Figure S3). Similar observations were made for **[C_2mim]Fe-1.5**, but precipitation occurred over a longer period of time, on the order of a few weeks (Figure S4). This behaviour has already been described in the literature for chloroferrate ILs and is explained by the fact that additional iron(III) chloride does not dissolve completely and eventually precipitates out, the energy of formation of $[Fe_2Cl_7]^-$ being lower than the lattice energy of $FeCl_3$.[43]

DSC thermograms of the three ILs of the **[C_2mim]Fe-x** series showed very different behaviours (Figure 1c-e). **[C_2mim]Fe-0.5** showed a glass transition, T_g, at – 63 °C (onset at second heating, Figure 1c) with a quantity of heat of – 20.7 $J.g^{-1}$. **[C_2mim]Fe-1** and **[C_2mim]Fe-1.5** showed melting points, T_m, at 17 and 1 °C, respectively (onset at second heating, Figure 1d-e), with heats of fusion of – 69.6 and – 36.3 $J.g^{-1}$, respectively. A weak solid-solid phase transition was also observed at – 16 °C (onset at second heating, Figure 1d) for **[C_2mim]Fe-1** which is consistent with the literature.[37-38] These observations suggest greater interionic interactions in **[C_2mim]Fe-1** and **[C_2mim]Fe-1.5** compared to **[C_2mim]Fe-0.5**.

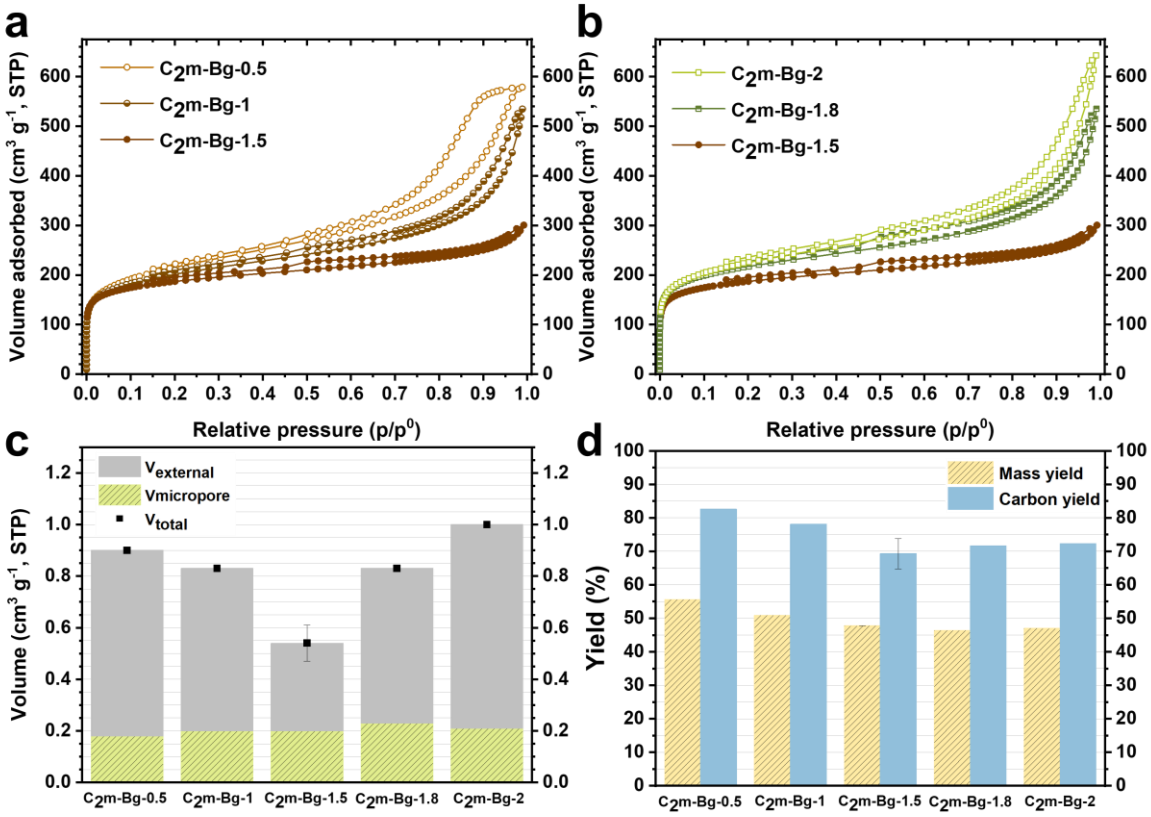

Figure 2. (a) Nitrogen sorption isotherms at 77 K of **C_2m-Bg-0.5**, **C_2m-Bg-1**, **C_2m-Bg-1.5**. (b) Nitrogen sorption isotherms at 77 K of of **C_2m-Bg-1.5**, **C_2m-Bg-1.8**, **C_2m-Bg-2**. (c) Total, external and micropore volumes of the five ionochars of the **C_2m-Bg-x** series. The micropore volumes were determined from the t-plot method (Thickness equation: Harkins and Jura). (d) Mass (corrected) and carbon yields of the five ionochars of the **C_2m-Bg-x** series.

After studying their anion speciation and phase transition behaviour, these **[$C_n$mim]Fe-x** ILs were used for the ITC of sugarcane bagasse and cellulose. The reactions were carried out at 240 °C for 20 h. The ionochars prepared from sugarcane bagasse were named **C_nm-Bg-x**, while the ones prepared from cellulose were named **C_nm-C-x**, with n, the alkyl chain length in $[C_nmim]^+$, and x, the $FeCl_3$/$[C_nmim]Cl$ molar ratio. The ITC of sugarcane bagasse was first performed in the **[C_2mim]Fe-x** series, with n = 2. As mentioned above, five different 1-ethyl-3-

methylimidazolium chloroferrate ILs with molar ratios ranging from 0.5 to 2 were prepared, yielding five **C_2m-Bg-x** ionochars. Their textural properties were determined by nitrogen gas sorption at 77 K. Significant differences were observed. The nitrogen sorption isotherm obtained for **C_2m-Bg-0.5** displays a type I/IV isotherm with a H1-type hysteresis loop (Figure 2a), characteristic of micro-mesoporous materials with an open geometry and a narrow range of mesopore sizes[46]. The shape of the isotherms changes significantly from **C_2m-Bg-0.5** to **C_2m-Bg-1.5** (Figure 2a). **C_2m-Bg-1** and **C_2m-Bg-1.5** display type I/II isotherms with a H3- to H4-type hysteresis loop (Figure 2a), characteristic of porous materials with micro-, meso- and macropores. This feature is accompanied by a decrease in the total pore volume. Thus, when increasing the $FeCl_3$/[C_2mim]Cl molar ratio from 0.5 to 1.5, the total pore volume gradually decreases from 0.9 cm^3 g^{-1} for **C_2m-Bg-0.5** to 0.54 cm^3 g^{-1} for **C_2m-Bg-1.5** (Table 1). When increasing the $FeCl_3$/[C_2mim]Cl molar ratio from 1.5 to 2, the opposite trend is observed. The total pore volume gradually increases from 0.54 cm^3 g^{-1} for **C_2m-Bg-1.5** to 1 cm^3 g^{-1} for **C_2m-Bg-2** (Table 1), while the shape of the hysteresis loops changes from a H4- to a H3-type (Figure 2b). When representing the evolution of both external and micropore volumes of the **C_2m-Bg-x** series (Figure 2c), one may notice that the micropore volume varies only slightly as a function of the $FeCl_3$/[C_2mim]Cl molar ratio, whatever the method used to determine it, *i.e.*, t-plot or 2D-NLDFT (Table S1 and Figure S5). Therefore, while the contribution of the external pore volume reaches a minimum for **C_2m-Bg-1.5**, the micropore contribution reaches a maximum for this ionochar.

The chemical structure of the **C_2m-Bg-x** series was investigated by Raman spectroscopy (Figure S6), FTIR (Figure 3a, Figure S7) and ^{13}C solid-state CP-MAS NMR (Figure 3b). The five ionochars display similar Raman spectra that are typical of amorphous carbonaceous

structures with a significant fraction of sp^3-hybridized carbon atoms and the presence of small aromatic clusters (Figure S6). They also present similar FTIR spectra (Figure 3a) with five bands centered at 1700 (C=O stretching vibrations of aromatic carbonyl groups), 1600 and 1440 (aromatic C=C stretching vibrations), 1374 (CH_3 bending vibrations of aromatic methyl groups) and 1220 cm^{-1} (C–O stretching vibrations in aromatic ethers and esters). Only one significant difference can be noted for **C_2m-Bg-0.5** that shows a band at *ca.* 1020-1220 cm^{-1} related to stretching vibrations of C–N bonds that may come from residual imidazole moieties. This band is less intense for **C_2m-Bg-x** with $x \geq 1$ (Figure 3a, Figure S7). ^{13}C CP-MAS solid-state NMR spectrum (Figure 3b) showed two major contributions: the aliphatic region between 0 and 30 ppm and the aromatic region centered at 120-130 ppm. The aliphatic contribution, centered at *ca.* 12 ppm, was more intense for **C_2m-Bg-0.5** and may suggest the partial degradation of the imidazolium cation during ITC. Furthermore, the shoulder centered at ca. 150 ppm that can be attributed either to aromatic carbons bounded to lignin methoxy groups or to polyfuranic structures, was less intense for **C_2m-Bg-0.5** than for **C_2m-Bg-1** and **C_2m-Bg-1.5**. Although still open to discussion, chloroferrate anions may coordinate to oxygen atoms of lignocellulose and stabilize oxygen groups of ionochars.[24]

Another important feature was observed with mass and carbon yields (Figure 2d). Both yields decreased when increasing the $FeCl_3$/[C_2mim]Cl molar ratio from 0.5 to 1.5, before reaching a plateau. Besides, elemental analyses performed on **C_2m-Bg-0.5** showed higher nitrogen contents as compared to the four other ionochars of the **C_2m-Bg-x** series (Table 1). This behaviour, also highlighted by FTIR and ^{13}C solid-state NMR spectroscopy, can be explained by the lowest thermochemical stability of **[C_2mim]Fe-0.5** and its degradation in imidazole moieties during ITC at 240 °C.

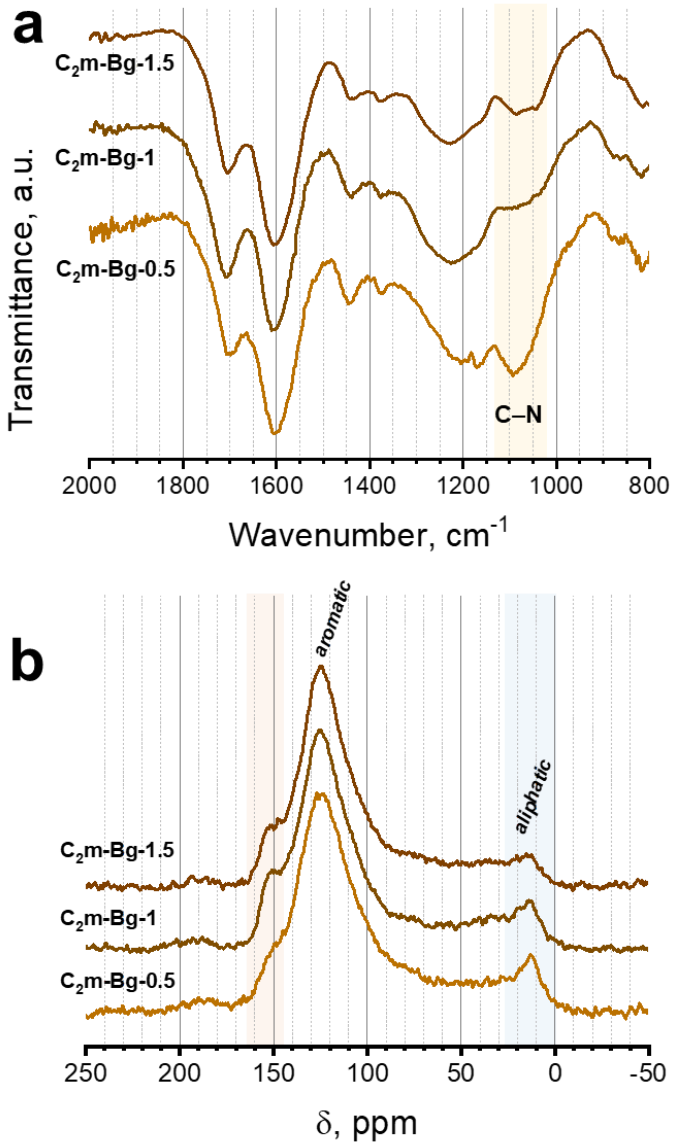

Figure 3. (a) FTIR spectra of **C_2m-Bg-0.5**, **C_2m-Bg-1** and **C_2m-Bg-1.5**. (b) ^{13}C CP-MAS solid-state NMR spectra of **C_2m-Bg-0.5**, **C_2m-Bg-1** and **C_2m-Bg-1.5**.

Table 1. Yields, elemental compositions and textural properties of the different ionochars reported herein.

Ionochars	Y_{mc} (wt%)[a]	Y_c (%)[b]	N/C[c]	Fe (wt%)[d]	Cl (wt%)[d]	SSA_{BET} ($m^2\ g^{-1}$)	SSA_{micro} ($m^2\ g^{-1}$)[e]	V_{total} ($cm^3\ g^{-1}$)[f]	V_{ext} ($cm^3\ g^{-1}$)[e]
C_2m-Bg-0.5	53.1	82.6	0.0169	1.5	2.3	777	403	0.90	0.72
C_2m-Bg-1	50.8	78.1	0.0026	2.3	1.7	734	467	0.83	0.63
C_2m-Bg-1.5	47.1	69.3	0.0058	2.5	2.7	663	477	0.54	0.34
C_2m-Bg-1.8	46.1	71.6	0.0038	1.1	2.9	792	532	0.83	0.6
C_2m-Bg-2	46.8	72.3	0.0029	2.4	2.2	819	497	1.00	0.79
C_2m-C-0.5	50.5	83.5	0.0116	0.3	1.5	982	450	1.47	1.27
C_2m-C-1	49.0	79.4	0.0012	0.0	1.9	842	514	0.81	0.59
C_4m-Bg-0.5	56.6	89.5	0.0072	3.0	2.1	619	350	0.50	0.35
C_4m-Bg-1	52.2	81.9	0.0044	1.2	2.4	628	495	0.46	0.25
C_6m-Bg-0.5	56.4	92.7	0.0094	0.8	1.7	601	345	0.48	0.33
C_6m-Bg-1	51.7	79.2	0.0040	3.9	2.7	518	396	0.31	0.14
C_8m-Bg-0.5	53.4	85.3	0.0133	1.5	1.8	500	272	0.39	0.27
C_8m-Bg-0.5-L	57.1	94.7	0.0096	0.0	1.1	545	193	1.07	0.98
C_8m-Bg-1	52.6	80.3	0.0065	3.3	2.0	242	183	0.13	0.06

[a]Y_{mc} for corrected mass yield; [b]Y_c for carbon yield; [c]Molar ratios obtained from elemental analyses; [d]SEM-EDX analyses; [e]Determined from the t-plot method (Thickness equation: Harkins and Jura); [f]Determined from the amount of nitrogen adsorbed at a relative pressure of 0.99.

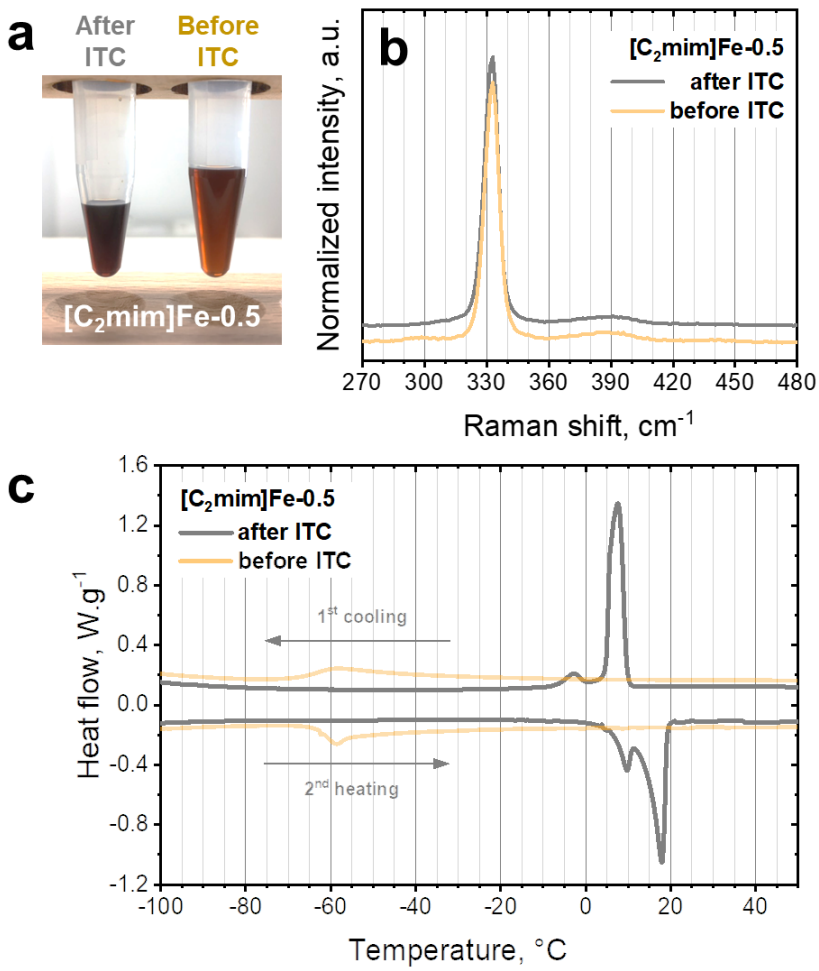

Figure 4. Chemical stability of **[C_2mim]Fe-0.5** IL. (a) Picture, (b) Raman spectra and (c) DSC thermograms of **[C_2mim]Fe-0.5** before and after ITC of sugarcane bagasse at 240°C for 20 hours.

To further confirm these features, both **[C_2mim]Fe-0.5** and **[C_2mim]Fe-1** were recovered after ITC of sugarcane bagasse at 240 °C for 20 h. Recovered ILs are slightly darker (Figure 4a), suggesting the presence of residual by-products. Interestingly, the Raman spectra of the two recovered ILs (Figure 4b, Figure S8) showed very similar peaks as those of the pristine ILs, with an intense peak centred at 333 cm^{-1} and a weaker contribution at *ca.* 390 cm^{-1}. This observation

supports that the tetrachloroferrate anions remained intact after ITC. However, DSC thermograms of **[C_2mim]Fe-0.5** before and after ITC are very different (Figure 4c). The T_g of the pristine IL at – 63 °C disappeared, while a T_m appeared at 14 °C (onset at second heating), supporting a radical change in the nature of the IL. The thermogram of **[C_2mim]Fe-0.5** after ITC resembles that of **[C_2mim]Fe-1** (Figure 1d) which could indicate an increase in the chloroferrate/1-ethyl-3-methylimidazolium ratio due to partial degradation of the cation during ITC. GC-MS analyses carried out on **[C_2mim]Fe-0.5** recovered after ITC, revealed the presence of residual imidazole moieties (Figure S9), confirming a partial thermal degradation of the 1-ethyl-3-methylimidazolium cation.[47] Unlike **[C_2mim]Fe-0.5**, no imidazole fragments were observed for **[C_2mim]Fe-1** recovered after ITC. The low thermal stability of **[C_2mim]Fe-0.5** compared to **[C_2mim]Fe-1** and **[C_2mim]Fe-1.5** was confirmed by thermogravimetric analyses (Figure S10).

ITC was also carried out with commercial cellulose, which is the main constituent of sugarcane bagasse. Similar trends were observed (Figure 5a, Table 1). **C_2m-C-0.5** displays a type I/IV isotherm with a H1-type hysteresis loop, while **C_2m-C-1** displays a type I/II isotherms with a H3-type hysteresis loop (Figure 5a). The total pore volume increases from 0.81 $cm^3\ g^{-1}$ for **C_2m-C-1** to 1.47 $cm^3\ g^{-1}$ for **C_2m-C-0.5**. Simultaneously, the contribution of micropores in both pore volume and specific surface area decreased from **C_2m-C-1** to **C_2m-C-0.5** (Figure 5a, Table 1). In the same way as for bagasse, both mass and carbon yields slightly increased from **C_2m-C-1** to **C_2m-C-0.5** (Table 1). This result indicates that the observed trends are not specific to sugarcane bagasse and that the approach could also be applied to other cellulose-rich agrowastes.

To further support the role of the chloroferrate anion, ITC of bagasse was also carried out in **[$C_n$mim]Fe-x** with longer alkyl chains ($n \geq 4$). Comparable trends were observed. **C_nm-Bg-**

0.5 showed higher yields, higher nitrogen content and the presence of residual imidazole moieties was revealed by FTIR (Figures S11-13). Moreover, **C_nm-Bg-0.5** ionochars systematically display a type I/IV isotherm with a H2a-type hysteresis loop, while **C_nm-Bg-1** ionochars systematically display a type I/II isotherms with a H3-type hysteresis loop (Figure 5b-d). Note that the H2a-type hysteresis loops observed for the **C_nm-Bg-0.5** ionochars with $n \geq 4$ are characteristic of micro-mesoporous materials with pore restrictions or with narrow pore entrances, such as ink-bottle-shaped pore networks[46]. This difference between pore networks in **C_2m-Bg-0.5** and in the three other **C_nm-Bg-0.5** ionochars is in good agreement with our previous study on the role of the cation on textural and morphological properties.[26] As the length of the alkyl chain increases, the ability of 1-alkyl-3-methylimidazolium chloroferrate ILs to dissolve lignocellulose becomes increasingly weak leading to ionochars with more restricted pore networks. We invite the readers to refer to our previous works for a comprehensive overview regarding the impact of the cationic structure on the ITC of (ligno)cellulose.[26]

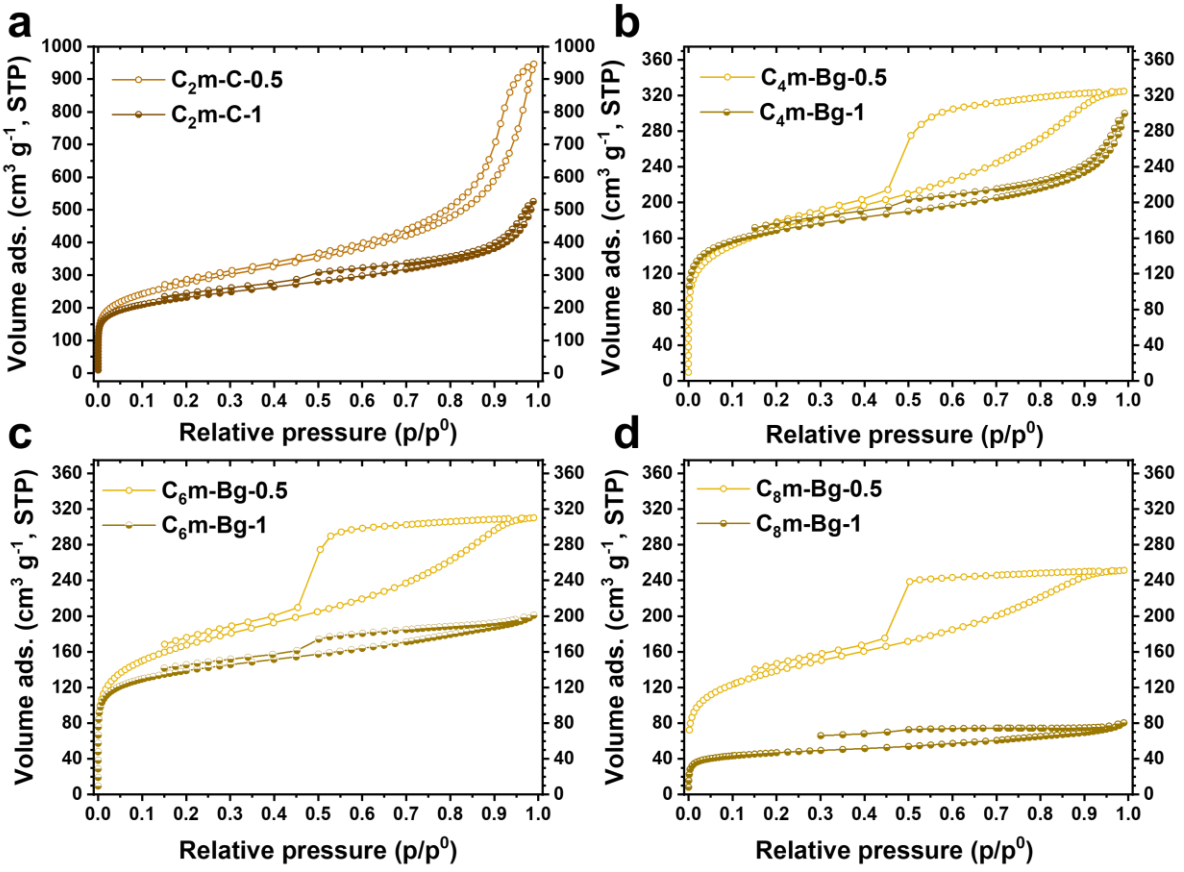

Figure 5. Nitrogen sorption isotherms at 77 K of (a) **C_2m-C-0.5** versus **C_2m-C-1**, (b) **C_4m-Bg-0.5** versus **C_4m-Bg-1**, (c) **C_6m-Bg-0.5** versus **C_6m-Bg-1**, (d) **C_8m-Bg-0.5** versus **C_8m-Bg-1**.

Overall, we showed that the external pore volume contribution systematically increases from **C_nm-Bg-1** to **C_nm-Bg-0.5**, whatever the method used to determine it, *i.e.*, t-plot (Figure 6a) or 2D-NLDFT (Table S1 and Figure S14). This behavior is more pronounced for cellulose (**C_2m-C-x** versus **C_2m-Bg-x**) and imidazolium cations with longer alkyl chain. However, as mentioned above, the **C_nm-Bg-0.5** ionochars with $n \geq 4$ display H2a-type hysteresis loops suggesting complex pore networks with pore restrictions.[46] One may assume that pore restrictions are due to the drying method used herein, *i.e.*, oven-drying, which might generate a huge shrinkage of the pore network due to capillary forces. To support this statement, a ionochar prepared in

[C_8mim]Fe-0.5 was dried by freeze-drying, yielding **C_8m-Bg-0.5-L**. Before freeze-drying, the ionochar was washed several times in an aqueous solution with 25 wt% of *tert*-butyl alcohol to avoid ice crystal growth and to preserve the nanostructure.[48] Note that self-standing monolithic gels were systematically obtained when conducting ITC of bagasse in the **[C_8mim]Fe-0.5** IL (Figure 6b, insert). Interestingly, **C_8m-Bg-0.5-L** displays a type I/II isotherm with a H3-type hysteresis loop (Figure 6b). As anticipated, the pore volume increased from 0.39 cm^3 g^{-1} for the oven-dried ionochar, **C_8m-Bg-0.5**, to 1.07 cm^3 g^{-1} for the freeze-dried ionochar, **C_8m-Bg-0.5-L**, mainly due to the contribution of the external pore volume. This feature was further confirmed by scanning (SEM; Figure 6c-d) and transmission (TEM; Figure S15) electron microscopy. Similar observations were made with cellulose treated in **[C_6mim]Fe-0.5**, yielding **C_6m-C-0.5** (oven-dried) and **C_6m-C-0.5-L** (freeze-dried; Figure S16).

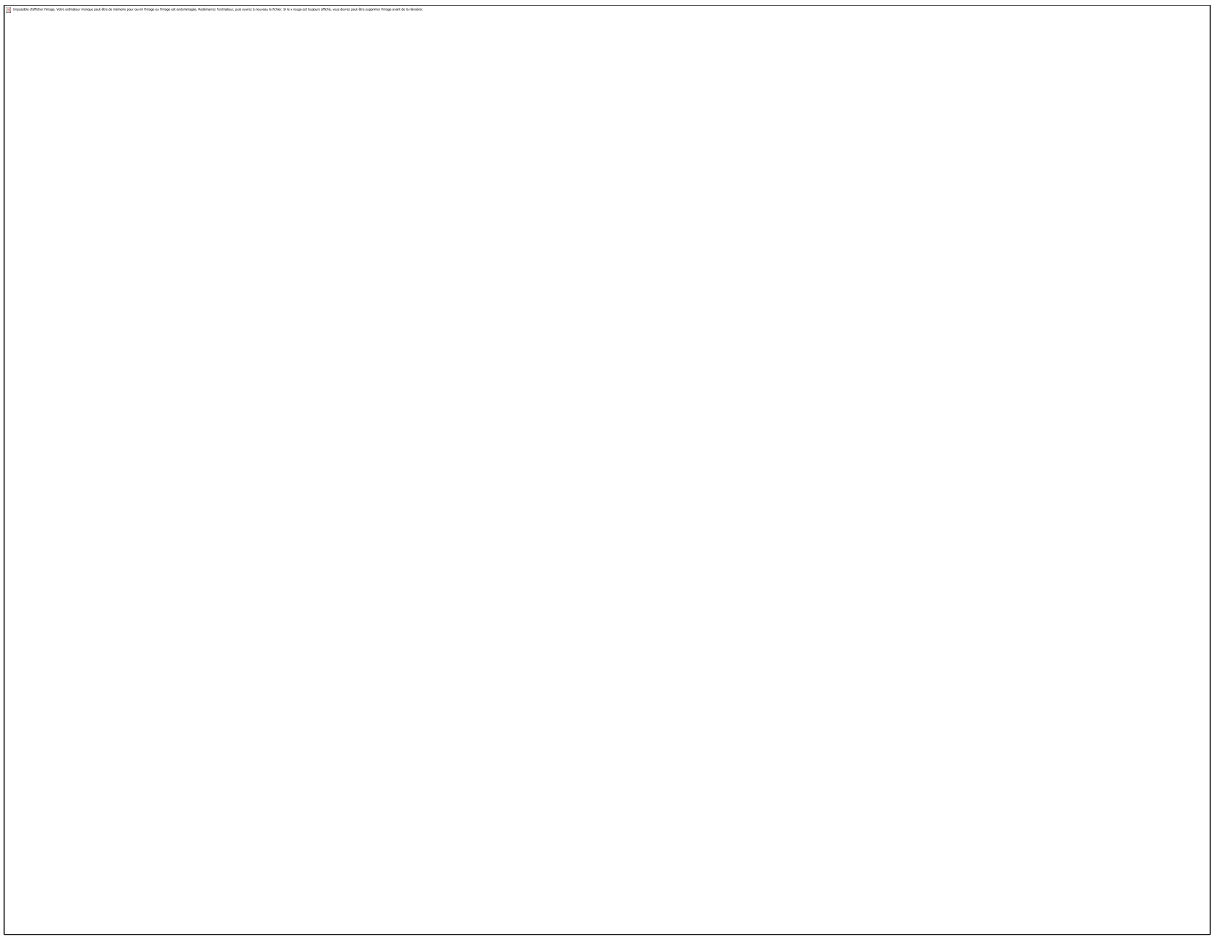

Figure 6. (a) Comparison of the V_{ext}/V_{total} ratios for the different ionochars prepared herein at x = 0.5 and 1. The external pore volumes, V_{ext}, were determined from the t-plot method (Thickness equation: Harkins and Jura). (b) Nitrogen sorption isotherms at 77 K of **C_8m-Bg-0.5-L** (freeze-dried) versus **C_8m-Bg-0.5** (oven-dried). Insert: picture of a wet gel of ionochar **C_8m-Bg-0.5** just before drying. SEM micrographs of (c) **C_8m-Bg-0.5** (oven-dried) versus (d) **C_8m-Bg-0.5-L** (freeze-dried).

In our previous study, we demonstrated the possibility to control both textural and morphological properties of ionochars through cation engineering.[26] Herein, we showed that the chloroferrate anion has also a strong impact on textural properties. Interestingly, we also showed a fine control in terms of morphological properties. Indeed, significant differences were observed

in the **C_2m-Bg-x** series (Figure 7). The two ionochars prepared in ILs with the lowest $FeCl_3$/[C_2mim]Cl molar ratios, *i.e.*, **C_2m-Bg-0.5** and **C_2m-Bg-1**, are made of aggregates of small nanoparticles. SEM and TEM micrographs reveal an interconnected pore network made of large mesopores and narrow macropores (Figures 7a-b). This feature is in good agreement with the data extracted from the nitrogen sorption analyses (Figure 2a; Table 1). When increasing the $FeCl_3$/[C_2mim]Cl molar ratio, *i.e.*, for **C_2m-Bg-1.5**, **C_2m-Bg-1.8** and **C_2m-Bg-2**, very different morphologies were obtained (Figures 7c-e). In addition to aggregates of small nanoparticles, TEM micrographs reveal hollow fibers, *i.e.*, nanotubes, the inner diameter of the tubes being clearly identified (Figure $7c_1$-e_1). As mentioned above, ILs bearing anions with strong HBA ability are more likely to dissolve and depolymerize (ligno)cellulose. It is well known that chloride anions have a stronger HBA ability than tetrachloroferrate $[FeCl_4]^-$ and heptachlorodiferrate $[Fe_2Cl_7]^-$ anions. Thus, when $[FeCl_4]^-$ and $[Fe_2Cl_7]^-$ anions are predominant in 1-alkyl-3-methylimidazolium chloroferrate ILs, the dissolution/deconstruction of lignin is probably laborious. As a direct consequence, at high $FeCl_3$/[C_2mim]Cl molar ratios ($x > 1$) the lignocellulose-solvent interface is probably limited and the carbonization occurs in a heterogeneous solid-liquid biphasic medium. In the light of our previous work[26], one may assume that this feature allows preserving the fibrous structure of fibrils in lignocellulose and yields ionochar replicas made of hollow nanofibers. It should be noted that the occurrence of tubular nanostructures was more evident in **C_2m-Bg-1.5** than in **C_2m-Bg-1.8** and **C_2m-Bg-2**, especially by SEM (Figure $7c_1$-e_1). This feature might be due to the heterogeneity in 1-ethyl-3-methylimidazolium chloroferrate ILs with $FeCl_3$/[C_2mim]Cl molar ratios above 1.5. Besides, M.D. Nguyen *et al.*[49] showed that Fe(III) can be more easily reduced to Fe(II) and Fe(0) in $[Fe_2Cl_7]^-$ than in $[FeCl_4]^-$ species. Therefore, a mechanistic investigation and elucidation of ITC

in these ILs appears to be extremely complex. Overall, these observations are in agreement with the ones extracted from nitrogen sorption analyses. The ionochar with the highest occurrence of tubular nanostructures, *i.e.*, **C_2m-Bg-1.5**, displays the lowest external pore volume contribution (Figure 2c).

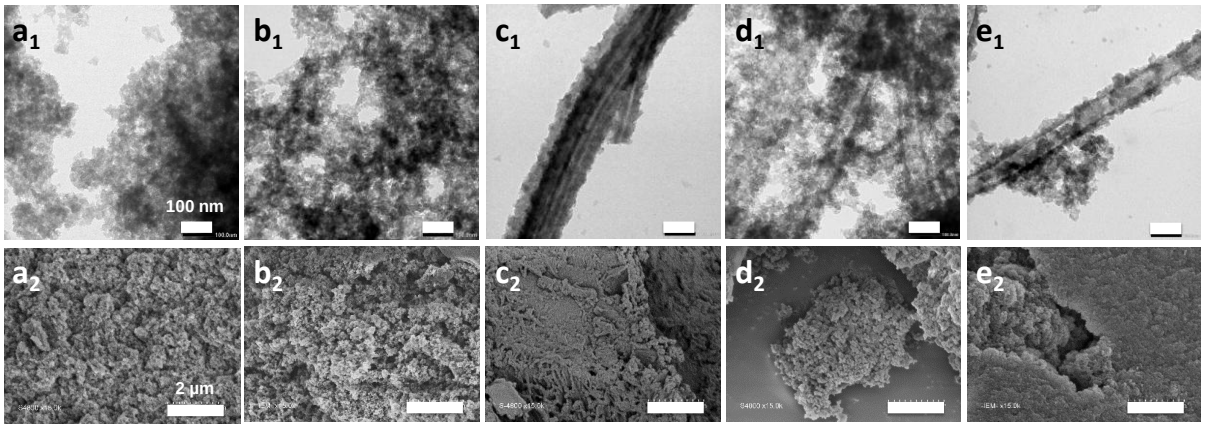

Figure 7. Micrographs obtained by transmission (a_1-e_1; scale bar 100 nm) and scanning (a_2-e_2; scale bare 2 µm) electron microscopy of (a) **C_2m-Bg-0.5**, (b) **C_2m-Bg-1**, (c) **C_2m-Bg-1.5**, (d) **C_2m-Bg-1.8** and (e) **C_2m-Bg-2**.

To better understand the interaction between lignocellulose and **[C_2mim]Fe-x** ILs, we performed immersion calorimetry with sugarcane bagasse in two different ILs, with x = 0.5 and 1.0 (Figure 8). For each IL, we obtained an exothermic peak that is related to the energy involved in bringing the sugarcane bagasse and the ionic liquid into contact through wetting and subsequent partial dissolution. We determined the enthalpy of immersion for each IL, *i.e.*, −32 ±4 $J.g^{-1}$ for **[C_2mim]Fe-0.5** and −4.5 ±1 $J.g^{-1}$ **[C_2mim]Fe-1**. This result supports the hypothesis that chloride anions are more likely to dissolve lignocellulose than tetrachloroferrate. It should be noted that similar experiments were performed with **[C_2mim]Fe-1.5**, containing heptachlorodiferrate anions. However, we observed intricate features, with low reproducibility, indicative of strong

and complex interactions between sugarcane bagasse and **[C$_2$mim]Fe-1.5** at low temperature. Heptachlorodiferrate anions are known to be more reactive than tetrachloroferrate anions,[50] which could favour hydrolysis and subsequent carbonization of (ligno)cellulose at low temperature. Additional characterization would be required to gain further insight.

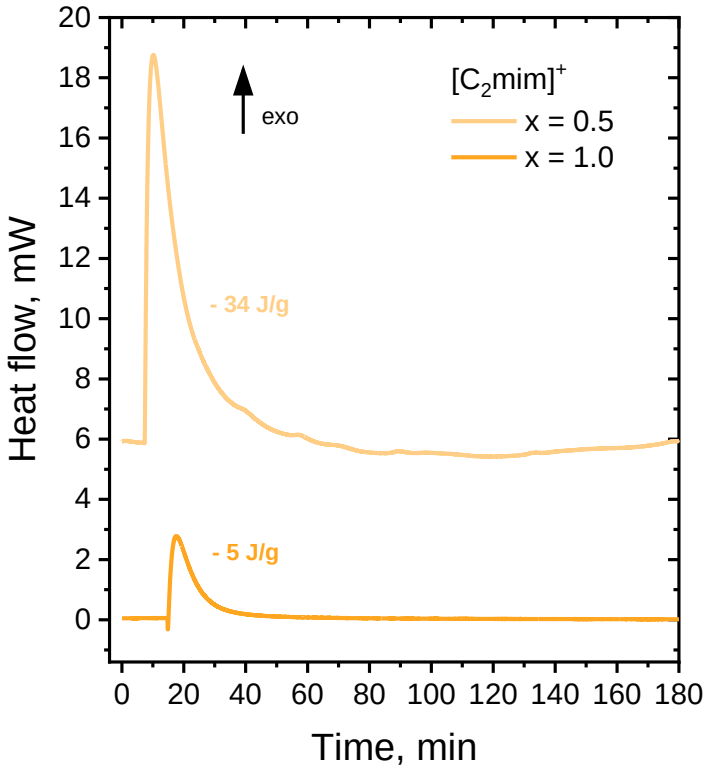

Figure 8. Heat flow over time obtained by immersion calorimetry of sugarcane bagasse in **[C$_2$mim]Fe-0.5** (upper curve; -34 J/g) and **[C$_2$mim]Fe-1** (bottom curve; -5 J/g).

The trends observed with the **C$_2$m-Bg-x** series were confirmed in **[C$_n$mim]Fe-x** with longer alkyl chains ($n \geq 4$; Figures S17-19). Tubular nanostructures were systematically obtained above a certain $FeCl_3$/[C$_x$mim]Cl molar ratio. The boundary between aggregates of small nanoparticles and tubular nanostructures gradually decreases from $x \approx 1.5$ for C_2 to $x \approx 1$ for C_8 (Figure 9). This feature highlights the concomitant role of the chloroferrate anion and the 1-alkyl-3-

methylimidazolium cation. On the one hand, shorter alkyl chains on the cation favour intermolecular interactions between the chloroferrate anions and (ligno)cellulose, which promote the dissolution of the latter. This aspect was thoroughly discussed in our previous work.[26] On the other hand, lower $FeCl_3$/[$C_n$mim]Cl molar ratios cause the prevalence of chloride anions, which have a stronger HBA ability, to the detriment of tetrachloroferrate $[FeCl_4]^-$ and heptachlorodiferrate $[Fe_2Cl_7]^-$ anions. The prevalence of chloride anions favours the dissolution of (ligno)cellulose, while the presence of the highly reactive heptachlorodiferrate anions promotes the chemical conversion of (ligno)cellulose. Thus, the concomitant role of the chloroferrate anion and the 1-alkyl-3-methylimidazolium cation provide a fine control over textural and morphological properties of ionochars that can be summarized as follows (Figure 9): (i) 1-alkyl-3-methylimidazolium chloroferrate ILs with short alkyl chains and/or low $FeCl_3$/[$C_n$mim]Cl molar ratios display strong interactions with (ligno)cellulose, yielding meso-macroporous ionochars made of aggregates of small nanoparticles; (ii) 1-alkyl-3-methylimidazolium chloroferrate ILs with long alkyl chains and/or high $FeCl_3$/[$C_n$mim]Cl molar ratios have greater difficulty dissolving (ligno)cellulose, yielding microporous ionochars made of tubular nanostructures.

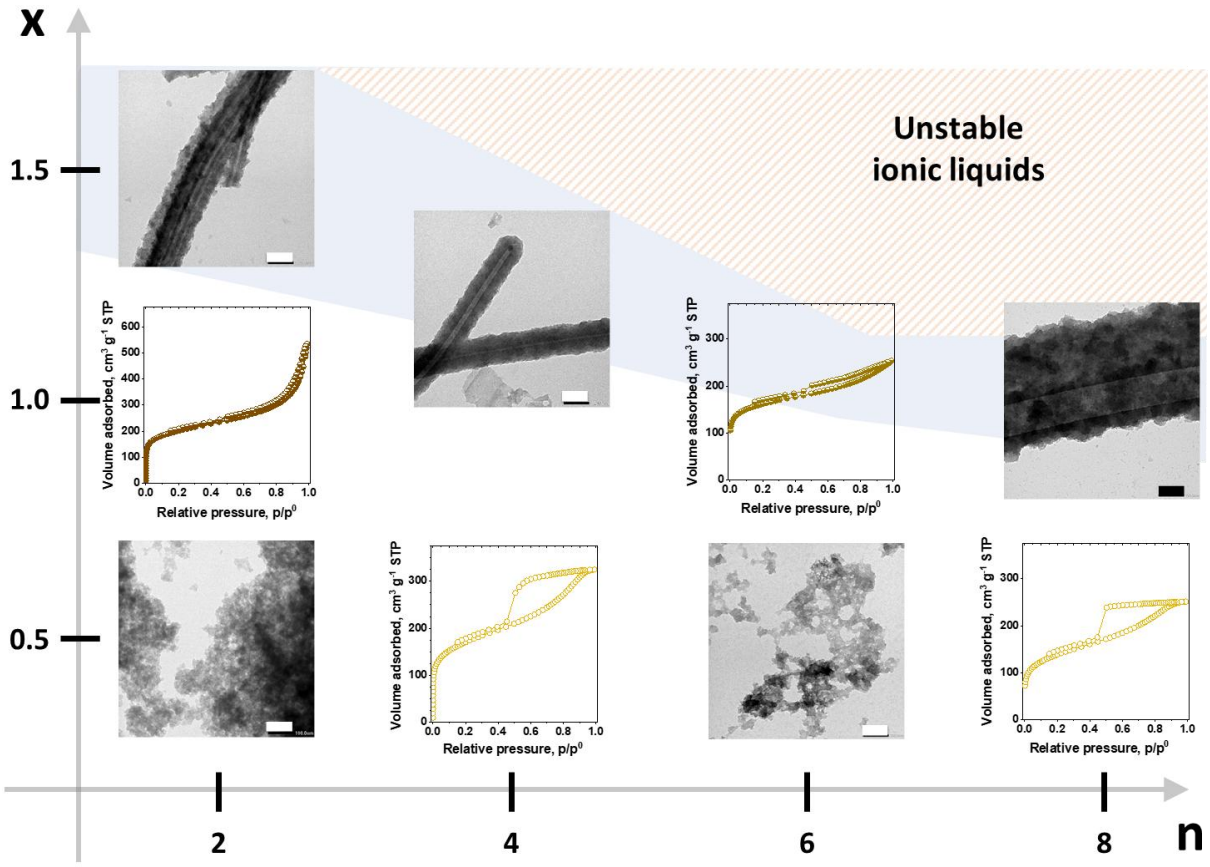

Figure 9. Schematic representation of the concomitant role of the chloroferrate anion and the 1-alkyl-3-methylimidazolium cation on both textural and morphological properties of ionochars. x, on the y-axis, corresponds to the $FeCl_3$/[$C_n$mim]Cl molar ratio and n, on the x-axis, corresponds to the length of the alkyl chain on the cation. The light blue area corresponds to the domain where microporous ionochars made of tubular nanostructures are obtained. The zebra area indicates the domain where heterogeneous ionic liquids are obtained. The nitrogen sorption isotherms at 77 K and the TEM micrographs are placed in the area corresponding to the synthesis conditions (x, n) of the associated ionochars. Scale bars on TEM micrographs: 100 nm.

The ionochars reported herein display high specific surface areas (up to 1 000 m^2 g^{-1}), high pore volumes (up to 1.5 cm^3 g^{-1}) and tuneable nanostructures. Due to these advantageous properties, they can find application in various fields, including wastewater treatment[51], electrocatalysis[22], electrochemical energy storage[23, 40] and environmental remediation[24]. In our previous study, we showed that cation engineering can significantly improve the CO_2 uptake, *i.e.*, the quantity of CO_2 adsorbed per gram of ionochar. Herein, we compared three ionochars of the **C_2m-Bg-x** series, *i.e.*, **C_2m-Bg-0.5**, **C_2m-Bg-1** and **C_2m-Bg-1.5** (Figure 10). The CO_2 uptake at 273.15 K of the three ionochars are very close: between 2.15 mmol of CO_2 per gram for **C_2m-Bg-0.5** and 2.4 mmol of CO_2 per gram for **C_2m-Bg-1.5** (Figure 10a). In the literature, it is known that the CO_2 adsorption capacity of carbonaceous materials is well correlated with the volume of micropores narrower than 0.7 nm, *i.e.*, the volume of ultramicropores.[52] To check this assumption, the micropore size distributions of **C_2m-Bg-0.5**, **C_2m-Bg-1** and **C_2m-Bg-1.5** were determined from the 2D-NLDFT models for porous carbons with heterogeneous surfaces using SAIEUS software (Figure S20).[53, 54] The absolute contribution in volume of ultramicropores (< 0.7 nm) and supermicropores (between 0.7 and 2 nm) and the corresponding volume fraction are represented for each ionochar of the **C_2m-Bg-x** series in Figure S21. A clear correlation can be made between ultramicropores and CO_2 uptake: the higher the contribution of ultramicropores (Figure S21, Figure 10b), the greater the CO_2 uptake. This correlation is particularly true at low pressures (Figure 10b), which is in agreement with other previous studies[52]. Besides, the isosteric heats of adsorption, which define the specific affinity for CO_2, were calculated using the Clausius-Clapeyron equation (see experimental section). Interestingly, the isosteric heat of adsorption does not follow the same trend as the CO_2 uptake; it increases following the order **C_2m-Bg-0.5** > **C_2m-Bg-1.5** > **C_2m-Bg-1** (Figure 10c). To understand this behavior, the role of

surface chemistry must be taken into account. On the one hand, the higher amount of residual nitrogen in **C_2m-Bg-0.5** (Table S1) might provide surface nitrogen functionalities that can act as basic sites with a great affinity for CO_2 molecules (which present a soft acidic character).[55] It is worth noting that the higher the N/C molar ratio (Table 1, Figure S22), the greater the isosteric heat of adsorption in absolute values. On the other hand, **C_2m-Bg-1**, and to a lesser extent **C_2m-Bg-1.5**, display higher O/C molar ratios than **C_2m-Bg-0.5** (Table S1, Figure S22). In the literature, it is known that oxygen functionalities can act as acidic sites that can be unfavorable to CO_2 adsorption.[55] This correlation seems to be confirmed here, since the higher the O/C molar ratio, the lower the isosteric heat of adsorption in absolute values (Figure 10d). This is particularly true at low pressures, *i.e.*, at low CO_2 uptakes (Figure 10d). These features, which are demonstrated for the first time with ionochars, confirm the concomitant roles of surface chemistry and textural properties of carbonaceous materials in CO_2 capture. Interestingly, our study demonstrates the versatility of the ionothermal process to design carbonaceous materials with singular properties. Therefore, it opens up new perspectives to engineer ILs able to conduct functionalization and ionothermal carbonization of agrowastes simultaneously.

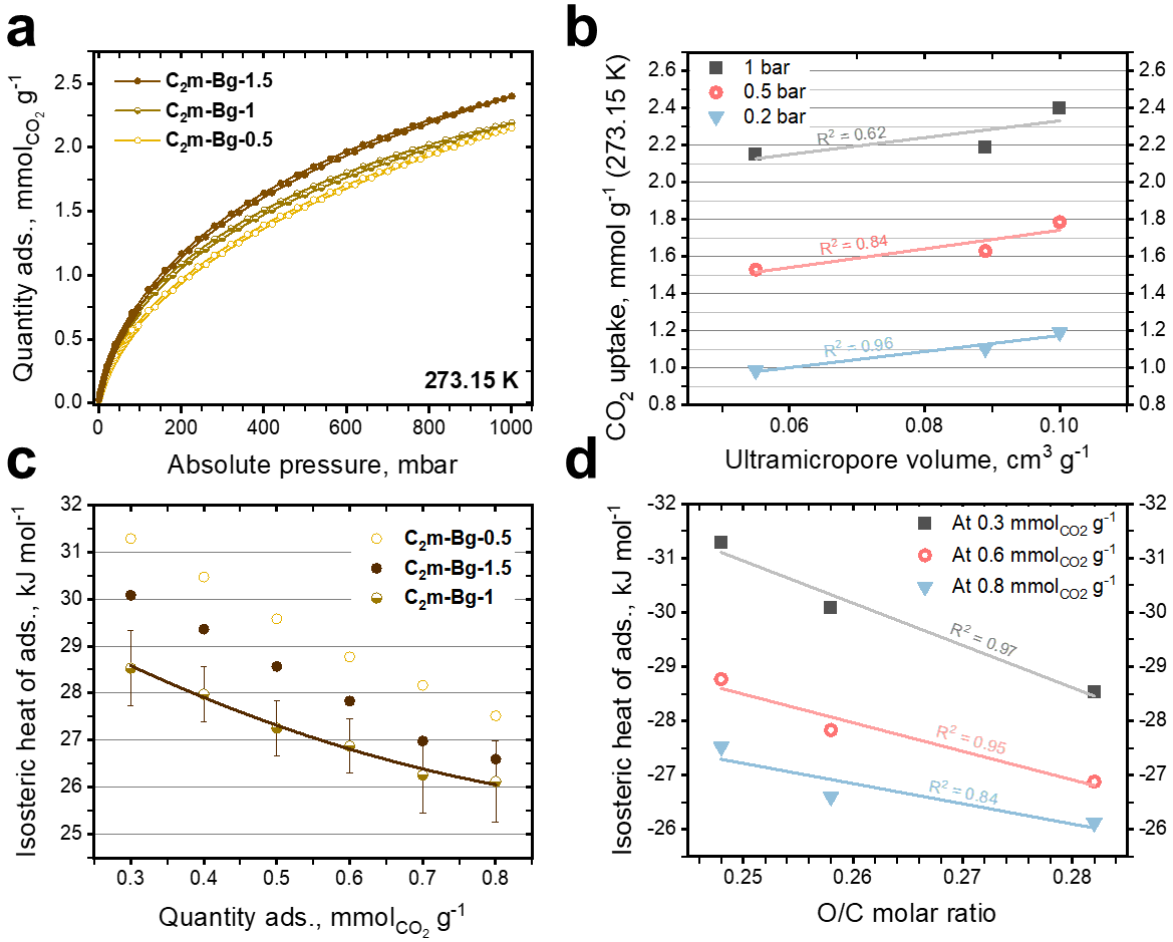

Figure 10. (a) Carbon dioxide sorption isotherms at 273.15 K of **C$_2$m-Bg-0.5**, **C$_2$m-Bg-1** and **C$_2$m-Bg-1.5**. (b) Correlation between CO_2 uptake at 273.15 K and ultramicropore volume for **C$_2$m-Bg-0.5**, **C$_2$m-Bg-1** and **C$_2$m-Bg-1.5**. Ultramicropore volumes were determined from the 2D-NLDFT models for porous carbons with heterogeneous surfaces using SAIEUS software[53,54]. (c) Isosteric heat of adsorption of CO_2 for **C$_2$m-Bg-0.5**, **C$_2$m-Bg-1** and **C$_2$m-Bg-1.5**. The isosteric heat of adsorption was calculated by applying the Clausius-Clapeyron equation to CO_2 adsorption isotherms obtained at three different temperatures (273.15, 298.15 and 323.15 K). The isosteric heats of adsorption are given as absolute values. (d) Correlation between O/C molar ratio determined from combustion elemental analyses and isosteric heat of adsorption for **C$_2$m-Bg-0.5**, **C$_2$m-Bg-1** and **C$_2$m-Bg-1.5**.

CONCLUSIONS

In summary, we propose an original and systematic study to fill the knowledge gap about the physico-chemical properties of 1-alkyl-3-methylimidazolium chloroferrate ILs and their use in the ionothermal carbonization of biomass. We identified anionic speciation and its impact on the properties of 1-ethyl-3-methylimidazolium chloroferrate ILs. We demonstrate that the ionothermal carbonization of (ligno)cellulose is a versatile process to produce advanced carbonaceous materials and to modulate their physico-chemical properties. We obtained ionochars with high specific surface area (up to 1 000 m^2 g^{-1}), high pore volume (up to 1.5 cm^3 g^{-1}), tuneable nanostructures and adjustable CO_2 uptake/retention properties. We highlight the concomitant role of the chloroferrate anion and the 1-alkyl-3-methylimidazolium cation, which can be summarized as follows: (i) 1-alkyl-3-methylimidazolium chloroferrate ILs with short alkyl chains and/or low $FeCl_3$/[$C_n$mim]Cl molar ratios display strong interactions with (ligno)cellulose, yielding meso- macroporous ionochars made of aggregates of small nanoparticles; (ii) 1-alkyl-3-methylimidazolium chloroferrate ILs with long alkyl chains and/or high $FeCl_3$/[$C_n$mim]Cl molar ratios have greater difficulty dissolving (ligno)cellulose, yielding microporous ionochars made of tubular nanostructures. Although the mechanisms involved in the ionothermal carbonization of (ligno)cellulose remain to be better understood, this process presents many advantages to engineer carbonaceous materials with adjustable properties.

ASSOCIATED CONTENT

Supporting Information. The supporting information is available free of charge and includes: Raman spectra of **[C_6mim]Fe-1**, Raman spectra of anhydrous $FeCl_3$, **[C_2mim]Fe-2** and **[C_2mim]Fe-1.5** versus time, FTIR and Raman spectra of **C_nm-Bg-x** ionochars, GC-MS spectra of **[C_2mim]Fe-0.5** recovered after ITC of sugarcane bagasse at 240 °C, TG/DTG analyses of **[C_2mim]Fe-x**, TEM and SEM micrographs of **C_nm-Bg-x**, **C_8m-Bg-0.5-L** and **C_6m-C-0.5-L** ionochars, nitrogen sorption isotherm at 77 K of **C_6m-C-0.5-L**, and micropore volumes determined from the 2D-NLDFT models.

AUTHOR INFORMATION

Corresponding Author

E-mail: nicolas.brun@enscm.fr

Nicolas Brun: 0000-0002-1013-311

Author Contributions

S.A.: Investigation, writing – original draft. A.G.: Investigation (DSC, TG/DTG and immersion calorimetry experiments). P.G.: Investigation (GC-MS experiments). M.E-S., S.K., I.B.M. and P.H.: Validation, writing – review & editing. A.M.: Funding acquisition, supervision, validation, writing – review & editing. N.B.: Conceptualization, funding acquisition, supervision, investigation, validation, writing – review & editing.

Funding Sources

This project was supported by Chimie Balard Cirimat Carnot institute through the ANR program N°16 CARN 0008-01. S.A. is grateful to Lebanese University for financial support.

Notes

There are no conflicts to declare.

ACKNOWLEDGMENT

S.A. is grateful to Lebanese University for financial support. The authors are grateful to the Ministry for Europe and Foreign Affairs and the Ministry of Higher Education and Research (Government of the French Republic) for financial support through the Hubert Curien Partnership programme (PHC IMHOTEP 2019, no. 41859SB). Several characterizations were performed with the support of the "Balard Plateforme d'Analyses et de Caractérisation (PAC Balard)". The authors would like to thank Didier Cot (IEMM, Univ. Montpellier, CNRS, ENSCM) for SEM analyses, Bertrand Rebière (ICGM, Univ. Montpellier, CNRS, ENSCM) for SEM-EDX analyses, Franck Godiard (MEA platform, Univ. Montpellier) for TEM analyses and Thierry Michel (L2C, Univ. Montpellier, CNRS) for his help with the Raman spectroscopy experiments. N.B. thanks Bénédicte Prelot and Jerzy Zajac (ICGM, Univ. Montpellier, CNRS, ENSCM) for their input and fruitful discussions on immersion calorimetry.

ABBREVIATIONS

ITC, ionothermal carbonization; IL, ionic liquid; HTC, hydrothermal carbonization; HBA, hydrogen-bond acceptance; DSC, differential scanning calorimetry; SEM; scanning electron microscopy: TEM, transmission electron microscopy; EDX, energy-dispersive X-ray spectroscopy.

REFERENCES

1. Brun, N.; Hesemann, P.; Esposito, D., Expanding the biomass derived chemical space. *Chemical Science* **2017,** *8* (7), 4724-4738.

2. Hu, B., K., Wang, L. Wu, S.-H. Yu, M. Antonietti, M.-M. Titirici, Engineering Carbon Materials from the Hydrothermal Carbonization Process of Biomass. *Adv. Mater* **2010,** *22*, 813.
3. Kubo, S.; Demir- Cakan, R.; Zhao, L.; White, R. J.; Titirici, M. M., Porous carbohydrate- based materials via hard templating. *ChemSusChem: Chemistry & Sustainability Energy & Materials* **2010,** *3* (2), 188-194.
4. Hu, S.; Zuo, S.; Xu, Z.; Han, C.; Shen, J., Mesoporous carbon materials prepared from carbohydrates with a metal chloride template. *Journal of Materials Chemistry* **2009,** *19* (41), 7759-7764.
5. Demir-Cakan, R.; Baccile, N.; Antonietti, M.; Titirici, M.-M., Carboxylate-rich carbonaceous materials via one-step hydrothermal carbonization of glucose in the presence of acrylic acid. *Chemistry of materials* **2009,** *21* (3), 484-490.
6. Titirici, M.-M.; Antonietti, M., Chemistry and materials options of sustainable carbon materials made by hydrothermal carbonization. *Chemical Society Reviews* **2010,** *39* (1), 103-116.
7. Makowski, P.; Cakan, R. D.; Antonietti, M.; Goettmann, F.; Titirici, M.-M., Selective partial hydrogenation of hydroxy aromatic derivatives with palladium nanoparticles supported on hydrophilic carbon. *Chemical Communications* **2008,** (8), 999-1001.
8. Liu, R.; Wu, D.; Feng, X.; Müllen, K., Nitrogen- doped ordered mesoporous graphitic arrays with high electrocatalytic activity for oxygen reduction. *Angewandte Chemie* **2010,** *122* (14), 2619-2623.
9. Demir-Cakan, R.; Makowski, P.; Antonietti, M.; Goettmann, F.; Titirici, M.-M., Hydrothermal synthesis of imidazole functionalized carbon spheres and their application in catalysis. *Catalysis Today* **2010,** *150* (1-2), 115-118.
10. Burchell, T.; Judkins, R.; Rogers, M.; Williams, A., A novel process and material for the separation of carbon dioxide and hydrogen sulfide gas mixtures. *Carbon* **1997,** *35* (9), 1279-1294.
11. Heuchel, M.; Davies, G.; Buss, E.; Seaton, N., Adsorption of carbon dioxide and methane and their mixtures on an activated carbon: simulation and experiment. *Langmuir* **1999,** *15* (25), 8695-8705.
12. Sudibandriyo, M.; Pan, Z.; Fitzgerald, J. E.; Robinson, R. L.; Gasem, K. A., Adsorption of methane, nitrogen, carbon dioxide, and their binary mixtures on dry activated carbon at 318.2 K and pressures up to 13.6 MPa. *Langmuir* **2003,** *19* (13), 5323-5331.
13. Meng, Y.; Gu, D.; Zhang, F.; Shi, Y.; Yang, H.; Li, Z.; Yu, C.; Tu, B.; Zhao, D., Ordered mesoporous polymers and homologous carbon frameworks: amphiphilic surfactant templating and direct transformation. *Angewandte Chemie International Edition* **2005,** *44* (43), 7053-7059.
14. Titirici, M.-M.; White, R. J.; Brun, N.; Budarin, V. L.; Su, D. S.; del Monte, F.; Clark, J. H.; MacLachlan, M. J., Sustainable carbon materials. *Chemical Society Reviews* **2015,** *44* (1), 250-290.
15. Lehmann, J., A handful of carbon. *Nature* **2007,** *447* (7141), 143-144.
16. Ouyang, J.; Zhou, L.; Liu, Z.; Heng, J. Y.; Chen, W., Biomass-derived activated carbons for the removal of pharmaceutical mircopollutants from wastewater: A review. *Separation and Purification Technology* **2020,** *253*, 117536.
17. Dubey, P.; Shrivastav, V.; Maheshwari, P. H.; Sundriyal, S., Recent advances in biomass derived activated carbon electrodes for hybrid electrochemical capacitor applications: Challenges and opportunities. *Carbon* **2020,** *170*, 1-29.

18. Fahmy, T. Y.; Fahmy, Y.; Mobarak, F.; El-Sakhawy, M.; Abou-Zeid, R. E., Biomass pyrolysis: past, present, and future. *Environment, Development and Sustainability* **2020,** *22* (1), 17-32.
19. Falco, C.; Baccile, N.; Titirici, M.-M., Morphological and structural differences between glucose, cellulose and lignocellulosic biomass derived hydrothermal carbons. *Green Chemistry* **2011,** *13* (11), 3273-3281.
20. Zhao, Y.-C.; Zhao, L.; Mao, L.-J.; Han, B.-H., One-step solvothermal carbonization to microporous carbon materials derived from cyclodextrins. *Journal of Materials Chemistry A* **2013,** *1* (33), 9456-9461.
21. Xie, Z.-L.; White, R. J.; Weber, J.; Taubert, A.; Titirici, M. M., Hierarchical porous carbonaceous materials via ionothermal carbonization of carbohydrates. *Journal of Materials Chemistry* **2011,** *21* (20), 7434-7442.
22. Zhang, P.; Gong, Y.; Wei, Z.; Wang, J.; Zhang, Z.; Li, H.; Dai, S.; Wang, Y., Updating biomass into functional carbon material in ionothermal manner. *ACS applied materials & interfaces* **2014,** *6* (15), 12515-12522.
23. Liu, Y.; Huang, B.; Lin, X.; Xie, Z., Biomass-derived hierarchical porous carbons: boosting the energy density of supercapacitors via an ionothermal approach. *Journal of Materials Chemistry A* **2017,** *5* (25), 13009-13018.
24. Cibien, L.; Parot, M.; Fotsing, P. N.; Gaveau, P.; Woumfo, E. D.; Vieillard, J.; Napoli, A.; Brun, N., Ionothermal carbonization in [Bmim][FeCl 4]: an opportunity for the valorization of raw lignocellulosic agrowastes into advanced porous carbons for CO 2 capture. *Green Chemistry* **2020,** *22* (16), 5423-5436.
25. Nicolae, S. A.; Au, H.; Modugno, P.; Luo, H.; Szego, A. E.; Qiao, M.; Li, L.; Yin, W.; Heeres, H. J.; Berge, N., Recent advances in hydrothermal carbonisation: from tailored carbon materials and biochemicals to applications and bioenergy. *Green Chemistry* **2020,** *22* (15), 4747-4800.
26. Aldroubi, S.; El-Sakhawy, M.; Kamel, S.; Hesemann, P.; Mehdi, A.; Brun, N., Ionothermal carbonization of sugarcane bagasse in imidazolium tetrachloroferrate ionic liquids: effect of the cation on textural and morphological properties. *Green Chem.* **2023,** *25*, 3533-3542.
27. Giernoth, R., Task- specific ionic liquids. *Angewandte Chemie International Edition* **2010,** *49* (16), 2834-2839.
28. Singh, S. K.; Savoy, A. W., Ionic liquids synthesis and applications: An overview. *Journal of Molecular Liquids* **2020,** *297*, 112038.
29. Cvjetko Bubalo, M.; Vidović, S.; Radojčić Redovniković, I.; Jokić, S., Green solvents for green technologies. *Journal of Chemical Technology & Biotechnology* **2015,** *90* (9), 1631-1639.
30. Swatloski, R. P.; Spear, S. K.; Holbrey, J. D.; Rogers, R. D., Dissolution of cellose with ionic liquids. *Journal of the American chemical society* **2002,** *124* (18), 4974-4975.
31. Salama, A.; Hesemann, P., Recent trends in elaboration, processing, and derivatization of cellulosic materials using ionic liquids. *ACS Sustainable Chemistry & Engineering* **2020,** *8* (49), 17893-17907.
32. Zhou, Y.; Zhang, X.; Yin, D.; Zhang, J.; Mi, Q.; Lu, H.; Liang, D.; Zhang, J., The solution state and dissolution process of cellulose in ionic-liquid-based solvents with different hydrogen-bonding basicity and microstructures. *Green Chemistry* **2022,** *24* (9), 3824-3833.
33. Li, Z.; Cai, Z.; Zeng, Q.; Zhang, T.; France, L. J.; Song, C.; Zhang, Y.; He, H.; Jiang, L.; Long, J., Selective catalytic tailoring of the H unit in herbaceous lignin for methyl p-

hydroxycinnamate production over metal-based ionic liquids. *Green Chemistry* **2018,** *20* (16), 3743-3752.
34. Mehta, M. J.; Kulshrestha, A.; Sharma, S.; Kumar, A., Room temperature depolymerization of lignin using a protic and metal based ionic liquid system: an efficient method of catalytic conversion and value addition. *Green Chemistry* **2021,** *23* (3), 1240-1247.
35. Ferrari, F.; Nogueira, G.; Franco, T.; Dias, M.; Cavaliero, C.; Witkamp, G. J.; Van Der Wielen, L.; Forte, M. B. S., The role of ionic liquid pretreatment and recycling design in the sustainability of a biorefinery: a sugarcane to ethanol example. *Green Chemistry* **2021,** *23* (22), 9126-9139.
36. Lungwitz, R.; Spange, S., A hydrogen bond accepting (HBA) scale for anions, including room temperature ionic liquids. *New Journal of Chemistry* **2008,** *32* (3), 392-394.
37. Yoshida, Y.; Saito, G., Influence of structural variations in 1-alkyl-3-methylimidazolium cation and tetrahalogenoferrate (III) anion on the physical properties of the paramagnetic ionic liquids. *Journal of Materials Chemistry* **2006,** *16* (13), 1254-1262.
38. Bäcker, T.; Breunig, O.; Valldor, M.; Merz, K.; Vasylyeva, V.; Mudring, A.-V., In-situ crystal growth and properties of the magnetic ionic liquid [C2mim][FeCl4]. *Crystal growth & design* **2011,** *11* (6), 2564-2571.
39. Jia, S.; Cox, B. J.; Guo, X.; Zhang, Z. C.; Ekerdt, J. G., Hydrolytic cleavage of β-O-4 ether bonds of lignin model compounds in an ionic liquid with metal chlorides. *Industrial & engineering chemistry research* **2011,** *50* (2), 849-855.
40. Baccour, M.; Louvain, N.; Alauzun, J. G.; Stievano, L.; Mutin, P. H.; Boury, B.; Monconduit, L.; Brun, N., Carbonization of polysaccharides in FeCl3/BmimCl ionic liquids: Breaking the capacity barrier of carbon negative electrodes in lithium ion batteries. *Journal of Power Sources* **2020,** *474*, 228575.
41. Sitze, M. S.; Schreiter, E. R.; Patterson, E. V.; Freeman, R. G., Ionic Liquids Based on FeCl3 and FeCl2. Raman Scattering and ab Initio Calculations. *Inorg. Chem.* **2001,** *40*, 2298-2304.
42. Li, J.-G.; Hu, Y.-F.; Sun, S.-F.; Ling, S.; Zhang, J.-Z., Ionic structures of nanobased FeCl3/[C4mim] Cl ionic liquids. *The Journal of Physical Chemistry B* **2012,** *116* (22), 6461-6464.
43. Estager, J.; Holbrey, J.; Swadźba-Kwaśny, M., Halometallate ionic liquids–revisited. *Chemical Society Reviews* **2014,** *43* (3), 847-886.
44. Clarke, C. J.; Baaqel, H. A.; Matthews, R. P.; Chen, Y.; Lovelock, K. R.; Hallett, J.; Licence, P., Halometallate Ionic Liquids: Thermal Properties, Decomposition Pathways, and Life Cycle Considerations. *Green Chemistry* **2022**, *24*, 5800-5812.
45. Nunes, L. J.; Loureiro, L. M.; Sá, L. C.; Silva, H. F., Sugarcane industry waste recovery: a case study using thermochemical conversion technologies to increase sustainability. *Applied Sciences* **2020,** *10* (18), 6481.
46. Thommes, M.; Kaneko, K.; Neimark, A. V.; Olivier, J. P.; Rodriguez-Reinoso, F.; Rouquerol, J.; Sing, K. S., Physisorption of gases, with special reference to the evaluation of surface area and pore size distribution (IUPAC Technical Report). *Pure and applied chemistry* **2015,** *87* (9-10), 1051-1069.
47. Chan, B. K. M.; Chang, N.-H.; Grimmett, M. R., The Synthesis and Thermolysis of Imidazole Quaternary Salts. *Aust. J. Chem.* **1977,** *30*, 2005 - 2013.
48. Borisova, A.; De Bruyn, M.; Budarin, V. L.; Shuttleworth, P. S.; Dodson, J. R.; Segatto, M. L.; Clark, J. H., A sustainable freeze- drying route to porous polysaccharides with tailored

hierarchical meso- and macroporosity. *Macromolecular rapid communications* **2015,** *36* (8), 774-779.
49. Nguyen, M. D.; Nguyen, L. V.; Jeon, E. H.; Kim, J. H.; Cheong, M.; Kim, H. S.; Lee, J. S., Fe-containing ionic liquids as catalysts for the dimerization of bicyclo [2.2. 1] hepta-2, 5-diene. *Journal of Catalysis* **2008,** *258* (1), 5-13.
50. Rodrigues, T. S.; Machado, F.; Micaroni Lalli, P.; Eberlin, M. N.; Neto, B. A. D., Styrene polymerization efficiently catalyzed by iron-containing imidazolium-based ionic liquids: Reaction mechanism and enhanced ionic liquid effect. *Catalysis Communications* **2015,** *63*, 66 - 73.
51. Xie, Z.-L.; Huang, X.; Titirici, M.-M.; Taubert, A., Mesoporous graphite nanoflakes via ionothermal carbonization of fructose and their use in dye removal. *RSC advances* **2014,** *4* (70), 37423-37430.

52. R. L. S. Canevesi; S. Schaefer; M. T. Izquierdo; A. Celzard; V. Fierro, Roles of Surface Chemistry and Texture of Nanoporous Activated Carbons in CO_2 Capture, *ACS Appl. Nano Mater.*, **2022**, *5*, 3843–3854.

53. J. Jagiello, Stable Numerical Solution of the Adsorption Integral Equation Using Splines, Langmuir, **1994**, *10*, 2778-2785.

54. J. Jagiello; J. P. Olivier, 2D-NLDFT Adsorption Models for Carbon Slit-Shaped Pores with Surface Energetical Heterogeneity and Geometrical Corrugation, *Carbon*, **2013**, *55*, 70-80.

55. Á. Sánchez-Sánchez; F. Suárez-García; A. Martínez-Alonso; J. M. D. Tascón, Influence of Porous Texture and Surface Chemistry on the CO_2 Adsorption Capacity of Porous Carbons: Acidic and Basic Site Interactions, *ACS Appl. Mater. Interfaces*, **2014**, *6*, 21237–21247.